Experimental study of the effect of noncondensables on buoyancy-thermocapillary convection in a volatile low-viscosity silicone oil

Y. Li, R. Grigoriev, and M. Yoda

Citation: Physics of Fluids (1994-present) **26**, 122112 (2014); doi: 10.1063/1.4904870
View online: http://dx.doi.org/10.1063/1.4904870
View Table of Contents: http://scitation.aip.org/content/aip/journal/pof2/26/12?ver=pdfcov
Published by the AIP Publishing

PHYSICS OF FLUIDS **26**, 122112 (2014)

Experimental study of the effect of noncondensables on buoyancy-thermocapillary convection in a volatile low-viscosity silicone oil

Y. Li,[1] R. Grigoriev,[2] and M. Yoda[1,a)]
[1]*G. W. Woodruff School of Mechanical Engineering, Georgia Institute of Technology, Atlanta, Georgia 30332-0405, USA*
[2]*School of Physics, Georgia Institute of Technology, Atlanta, Georgia 30332-0430, USA*

(Received 7 June 2014; accepted 5 December 2014; published online 30 December 2014)

The convective flow in a layer of volatile silicone oil with a kinematic viscosity of 0.65 cSt confined to a sealed cavity with a transverse aspect ratio of 3.2 was visualized using particle pathlines and quantified by particle-image velocimetry at dynamic Bond numbers estimated to be of order unity and laboratory Marangoni numbers as great as 3600. The effect of noncondensables (i.e., air) was studied by comparing convection in the liquid layer below a vapor space at pressures ranging from 4.8 kPa to 101 kPa, corresponding to air molar fractions ranging from 14% to 96%, respectively, and silicone-oil vapor, under otherwise identical conditions. The results for convection at 101 kPa are in qualitative agreement with previous studies, and clarify the time-dependent flow observed at high Marangoni numbers. The results show that decreasing the relative air concentration increases the critical Marangoni numbers for transition between different flow states, even though the air concentration does not appear to affect the speeds near the interface. Linear stability analysis shows that transitions are suppressed due to the latent heat generated or absorbed at the interface due to the enhancement of phase change. Furthermore, the experimental results suggest that air, even at relative concentrations as small as 14%, or partial pressures of $O(10^2$ Pa), has a significant effect on the vapor flow, and that the fluid in the vapor space should be modeled as a binary mixture in many cases of practical interest. © *2014 AIP Publishing LLC.* [http://dx.doi.org/10.1063/1.4904870]

I. INTRODUCTION

Compact thermal management technologies that can remove heat fluxes of O (100 W/cm^2) are required for cooling microelectronics, high-power microwave and radar systems, and space satellite systems, among other applications. Local heat fluxes over "hot spots" in microprocessors already exceed 300 W/cm^2,[1] and will likely exceed 1 kW/cm^2 within this decade.

Evaporative (i.e., two-phase) cooling, which takes advantage of the large latent heats associated with phase change, is one of the leading technologies for removing such high heat fluxes. Current passive two-phase cooling technologies include heat pipes, which are used to cool microprocessors in laptop computers, among other applications.[2,3] More recently, improved designs such as compact and lightweight micro-heat pipes using grooved channels with a hydraulic diameter of less than 0.1 cm, and oscillating or pulsating heat pipes where self-excited oscillations driven by vapor bubble dynamics enhance thermal transport, have been active areas of research.[4,5]

Fundamental to all of these devices is the nonisothermal flow, driven by capillary pressure due to the curvature of the liquid-vapor interface, or the pressure due to the expansion of vapor bubbles for oscillating heat pipes, from the (cold) condenser region to the (hot) evaporator region, of a liquid co-existing with its vapor in a confined and sealed cavity. In most cases, air is removed

a)Author to whom correspondence should be addressed. Electronic mail: minami@gatech.edu

from the cavity to minimize the effect of noncondensable gases on coolant phase change. The liquid evaporates in the hot region, removing heat, and the vapor then flows back towards the cold region, where it condenses, thereby transporting the heat from the hot to cold regions. The evaporation and condensation must balance in this sealed cavity. Since surface tension σ varies with temperature, any temperature gradient along the interface will give rise to thermocapillary (Marangoni) stresses. For the vast majority of simple (i.e., single-component) coolants, σ decreases as temperature increases, resulting in thermocapillary stresses that drive the liquid away from hot regions, which can change the wetting behavior and lead to film dryout, and hence adversely affect cooling performance.[6]

Despite numerous numerical and experimental studies, our fundamental understanding of the convective flow due to a temperature gradient in the presence of phase change remains limited. As noted by Schatz and Neitzel in their review of experimental investigations of thermocapillary instabilities,[7] most of the studies consider one of three flow configurations, namely cylindrical liquid bridges, rectangular layers, and annular geometries. These studies have focused on mapping out flow states in terms of the Marangoni number Ma (which describes the relative importance of thermocapillary and viscous effects) and characterizing flow transitions from two- to three-dimensional flow, from uni- to multi-cellular structures, and from steady to unsteady flows (e.g., traveling waves, oscillatory flow, or hydrothermal waves). The temperature gradient that defines the magnitude of thermocapillary stresses is the interfacial gradient $\tau_i \equiv \partial T_i/\partial x$, which is used to define the interfacial Marangoni number

$$Ma_i = \frac{\gamma h^2}{\mu\alpha}\tau_i, \tag{1}$$

where $\gamma = -\partial\sigma/\partial T$ is the surface tension temperature coefficient, h is the (average) depth of the liquid layer, μ is the liquid dynamic viscosity, and α is the thermal diffusivity of the liquid. However, most experimental studies use instead the laboratory Marangoni number[8]

$$Ma_L = \frac{\gamma h^2}{\mu\alpha}\frac{\Delta T}{L}, \tag{2}$$

based on the applied temperature difference ΔT, measured in some cases at the outer surface of the channel walls because of the practical difficulties in measuring the interfacial temperature without disturbing the flow, and the (longitudinal) dimension L of the liquid layer along the direction of the applied temperature difference. In general, $\Delta T/L$ is greater than τ_i (e.g., Ref. 9), and so $Ma_L > Ma_i$.

Burguete *et al.*[10] reviewed the studies of convection where both thermocapillarity and buoyancy are significant in rectangular layers. The relative importance of buoyancy and thermocapillary effects is given by the dynamic Bond number

$$Bo_D = \frac{\rho_L g\beta h^2}{\gamma}, \tag{3}$$

where ρ_L is the density and β is the thermal expansion coefficient of the liquid. Chan and Chen[11] have analyzed the effect of buoyancy, showing that at $Bo_D = O(1)$ it suppresses the hydrothermal waves predicted by the well-known stability analysis of Smith and Davis.[12]

Although many of the numerical studies, including stability analyses, of buoyancy-thermocapillary convection in liquid layers (reviewed in Ref. 11, for example) have considered effectively infinite liquid layers where h is much less than the other dimensions of the layer and the flow is 2D, experimental studies have clearly shown that 3D effects, characterized by the transverse aspect ratios $\Gamma_y \equiv W/h$ (where W is the transverse or cross-stream dimension of the liquid layer), could have a major effect on the flow.[9,10,13] Based on their comparisons with the earlier studies, Burguete *et al.*[10] concluded that the base flow was 2D for layers with $\Gamma_y > 10$ but that the flow would transition to traveling waves or steady multicellular structures (convection rolls) at small or large h (or Bo_D), respectively.

Table I, similar to Table I in Ref. 10, summarizes the experimental studies that have considered 3D convection in rectangular liquid layers at low transverse aspect ratios $\Gamma_y < 10$. Villers and Platten[14] reported that their flow evolved from a single convection roll to multiple convection rolls

TABLE I. Summary of experimental parameters for studies of rectangular liquid layers of small transverse aspect ratio Γ_y in chronological order.

References	Fluid	Dimensions (cm)			Γ_x	Γ_y	Maximum ΔT (°C)
		h	L	W			
14	Acetone	0.175–1.43	3	1	2.1–17	0.7–5.7	9
15	Silicone oil	0.68	1	3.8	1.5	5.6	20
9	Decane	0.25–0.47	3, 5, 7.4	1	6.4–30	2.1–4.0	9
13	Acetone	0.125–1	1.1	1.0	1.1–8.5	1.0–8.2	~20
17	Silicone oil; decane	0.2–0.35[10]	10	1	28–50	2.8–5	Not given

to a time-dependent flow as Ma increased. Gillon and Homsy[15] observed a transition from 2D to 3D convection in silicone oil with a kinematic viscosity $\nu = \mu/\rho_L = 0.65$ cSt at $Ma_L = 1.5 \times 10^5$. Braunsfurth and Homsy[13] showed in subsequent studies, however, that the critical Marangoni number for this transition was strongly dependent upon the longitudinal and transverse aspect ratios of the liquid layer $\Gamma_x \equiv L/h$ and Γ_y, respectively.

Much of the previous work cited here has focused on thermocapillary and buoyancy effects in liquid layers exposed to a large, and effectively infinite, volume of air at ambient conditions, and only a few studies have considered convection in volatile liquids. The experiments using acetone[13,14] studied convection in a(n at least partially) confined cell to minimize changes in h. Braunsfurth and Homsy[13] covered their flow cell with a "piece of glass and a silicone rubber seal," while Villers and Platten[14] used a Teflon block "a few millimetres above the upper surface" although no details were given regarding whether the cell was sealed by this block and whether acetone mass loss was negligible. In both of these cases, evaporation is therefore at least somewhat balanced by condensation, and phase change occurs in the presence of air at ambient pressures. Zhu and Liu[16] instead studied convection in a $L = 4$ cm and $W = 8$ cm layer of 0.65 cSt silicone oil subject to $\Delta T \leq 14$ °C with an initial depth $h = 0.2$ cm where the interface was open to the surroundings.

However, there are very few, if any (to our knowledge), studies of buoyancy-thermocapillary convection in a liquid layer for the situation most relevant to evaporative cooling: convection in a volatile liquid layer under its vapor in the (near-)absence of noncondensables confined to a sealed cavity with no change in net coolant mass so that the evaporation and condensation mass fluxes exactly balance. To our knowledge, nearly all of the numerical studies limit their scope to 2D convection under air at ambient pressures, use "one-sided" models that only consider transport in the liquid phase and, most importantly, ignore phase change and hence the associated latent heat released or absorbed at the interface. The simulations by Villers and Platten,[14] for example, did not account for heat and mass transfer above the liquid layer and imposed an adiabatic boundary condition at the liquid-vapor interface. The recent 2D study by Ji *et al.*[18] does consider phase change but under microgravity conditions and hence in the absence of buoyancy.

An experimental study was therefore performed of buoyancy-thermocapillary convection in a volatile silicone oil, hexamethyldisiloxane (HMDS), confined in a sealed rectangular cavity under a vapor space containing molar fractions of air C_a varying from 14% to 96%. The liquid layer had a dynamic Bond number $Bo_D \approx 0.7$, and a transverse aspect ratio $\Gamma_y \approx 4$ based on an average depth $\bar{h} \approx 0.25$ cm estimated from the experimental data and the analytical solution for this flow. Hexamethyldisiloxane was chosen because silicone oils are highly resistant to free-surface contamination, unlike common coolants such as water. The layer was subject to a horizontal temperature gradient created by applying temperature differences $\Delta T \leq 12.5$ °C (measured at the outer surface of the test cell) over $L = 4.85$ cm, corresponding to a range of $Ma_L = 290$–3600 based again on $\bar{h}$. Velocity fields were measured using two-dimensional two-component particle-image velocimetry (2D-2C PIV). The depth of the liquid layer and the interfacial temperature gradient were estimated, when appropriate, from a curve-fit of the measured horizontal velocity profile in the central section of the flow to the analytical solution for unidirectional 1D flow.

TABLE II. Properties of the volatile silicone oil hexamethyldisiloxane at 20 °C. Here, p_v is the vapor pressure and h_{fg} is the latent heat of vaporization.

ρ_L (kg/m^3)	μ (kg/(m s))	σ (N/m)	ν (m^2/s)	α (m^2/s)	β (K^{-1})	γ (N/(m K))	p_v (kPa)	h_{fg} [kJ/kg]
761	5.27×10^{-4}	0.0158	6.9×10^{-7}	7.5×10^{-8}	1.3×10^{-3}	8.9×10^{-5}	4.1	225

II. EXPERIMENTAL DESCRIPTION

A. Test cell and flow

The working fluid was the volatile silicone oil hexamethyldisiloxane (NMR grade with purity ≥99.5%, Sigma Aldrich 326739-100G) with the properties given in Table II and Prandtl number $Pr = \mu/(\rho_L \alpha) = 9.2$. The fluid was confined in a fused-quartz test cell (Starna Q1938) (inner dimensions 4.85 cm $(L) \times 1$ cm $(W) \times 1$ cm (H)) with two ports that was heated on its right end and cooled on its left end by thermoelectric Peltier devices (Custom Thermoelectric 01711-5L31-03CD) embedded in 1.4 cm × 1.4 cm × 0.6 cm copper blocks and powered by a dc power supply (Mastech HY3005-2) (Fig. 1). The test cell was mounted so that all four sides of the test cell were exposed to air at ambient conditions.

Two T-type thermocouples (TC) monitored the temperatures of the outer surfaces of the heated and cooled ends, T_h and T_c, respectively, with an accuracy of 0.2 °C. In this study, 21.7 °C ≤ T_h ≤ 28.6 °C and 14.9 °C ≤ T_c ≤ 20.8 °C, giving applied temperature differences $\Delta T \equiv T_h - T_c$ = 0.9 − 12.5 °C. The average of T_h and T_c was within 0.3 °C of the ambient temperature T_o, which varied between 20.0 °C and 21.3 °C, except at $\Delta T \geq 11.5$ °C, where the average was within 1.9 ° C of T_o. The temperature difference inside the end walls will be somewhat lower, since the thermal conductivity of quartz is small (~1.3 W/(m K)), which should be taken into account in comparison of the laboratory Marangoni number with other studies.

The silicone oil was seeded with fluorescent polystyrene (PS) particles (Invitrogen F8823) of diameter d = 1.1 μm and density ρ = 1.05 g/cm^3 at a nominal initial volume fraction $\phi = 4 \times 10^{-7}$. In all cases, the particle-laden solution was sonicated for 20 min to ensure that the tracers were well-dispersed in the fluid.

In all cases, the test cell was charged with ~3 ml of the particle-seeded solution, then evacuated by a vacuum pump (Edwards E-Lab 2) for ~2 min to a pressure of ~1.7 kPa, as monitored by a pressure transducer (Dwyer 626-23-GH-P1-E1-S4-NIST) with an accuracy of 0.26 kPa. The nominal average depth of the liquid layer, defined to be the volume of the liquid divided by the area LW, h_{av} = 0.31 cm, because about half of the HMDS is vaporized during this process, giving

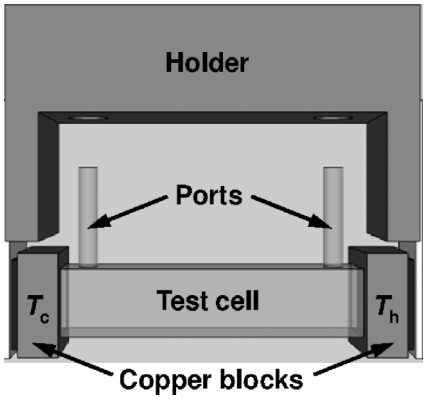

FIG. 1. Drawing of the the test cell (to scale); the heated and cooled ends are the right and left ends, respectively, in this view. The outer dimensions of the test cell, with a wall thickness of 0.125 cm, are 5.1 cm × 1.25 cm × 1.25 cm.

a transverse aspect ratio $\Gamma_y \equiv W/h_{av} = 3.2$. The capillary length scale $l_c \equiv [\sigma/(\rho_L g)]^{1/2} = 0.15$ cm (where g is the gravitational acceleration) for hexamethyldisiloxane at 20 °C, so $h_{av} \approx 2l_c$.

The minimum pressure in the vapor space p that could be achieved in these experiments was 4.83 kPa at $T_o = 20.3$ °C. This corresponds to a minimum $C_a = 14\%$, or an air partial pressure of 0.69 kPa, based on a vapor pressure for HMDS of 4.14 kPa at this value of T_o.[19] Higher relative air concentrations of $C_a = 36\%$, 57%, and 96% corresponding to $p = 6.59$ kPa, 10.1 kPa, and 101 kPa (i.e., ambient conditions), respectively, were achieved by letting air from the surroundings enter the test cell until p reached the desired value. Finally, the test cell was sealed by closing cut-off valves to prevent any mass loss during the actual experiments. In all cases, T_h and T_c reach their steady-state equilibrium values, i.e., vary by less than 0.2 °C over the duration of the entire experiment, and p_o reaches its steady-state value, i.e., varies by less than 0.2 kPa, 60–90 min after the start of heating and cooling.

B. Image acquisition

A 2D "slice" of the flow is illuminated by a laser light sheet (cross-sectional dimensions 0.04 cm × ~1.0 cm) at a wavelength $\lambda = 514.5$ nm. In the Cartesian coordinate system used here, x is along the horizontal pointing towards the cooled end, y is along the horizontal and the transverse direction, and z is along the vertical, with the origin at the bottom and center of the inner surface of the heated end of the test cell (Fig. 2). The interior of the test cell therefore occupies $0 \le x \le 4.85$ cm; -0.5 cm $\le y \le 0.5$ cm; and $0 \le z \le 1.0$ cm. The TCs that measure T_h and T_c are nominally at the centers of the end walls $(y, z) = (0, 0.5$ cm).

To obtain 2D-2C PIV measurements, the entire vertical central x-z plane of the flow at $y = 0$ was imaged within a single experimental run in these studies. This vertical plane was a composite of nine overlapping (typical overlap = 0.01 cm) 0.61 cm × 0.46 cm (653 × 492 pixels) views (Fig. 2(a)). Three horizontal $x - y$ planes of the flow at $z = 0.2$ cm, each a composite of six overlapping (overlap = 0.01 cm in x, 0.06 cm in y) 0.61 cm × 0.46 cm views (Fig. 2(b)), were also imaged in a separate experimental run under the same conditions.

The fluorescence from the particles was imaged through a bandpass filter (BrightLine FF01-542/27-25) that rejected the $\lambda = 514.5$ nm illumination and was recorded by an electron multiplying CCD camera (Photometrics Cascade 650) at a magnification of 0.79, or 9.4 μm per pixel. The laser beam was shuttered using an acousto-optic modulator (IntraAction Corp. AFM-803A1) to image the particles at an exposure time τ and a time interval between images within an image pair Δt. In all cases, a sequence of 200 16-bit image pairs (=400 images) with dimensions of 653 × 492

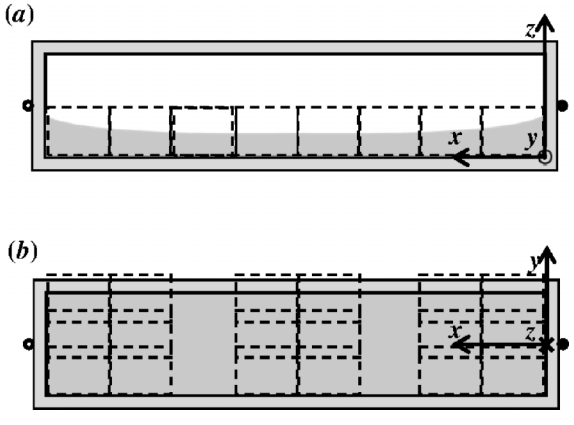

FIG. 2. Sketch of the test cell and the liquid layer defining the coordinate system and the views used for PIV in (a) the central vertical plane at $y = 0$ and (b) the horizontal plane at $z = 0.2$ cm. Each dashed rectangle indicates a single field of view of the camera, and the filled circle on the right and the open circles on the left indicate the nominal locations of the TCs used to measure T_h and T_c, respectively.

TABLE III. Summary of PIV image acquisition parameters.

ΔT (°C)	Plane	τ (ms)	Δt (ms)	$\mathcal{T}_T$ (s)
	C_a = 96%			
0.9, 1.4, 1.9, 3.0, 6.5, 7.8	Vertical	2	39	15.6
3.8	Vertical	2	20 or 40	60
3.8	Horizontal	2	39	15.6
11.5	Vertical	1	5	60
	C_a = 57%			
2.8	Vertical	2	39	15.6
3.9, 6.8, 9.8	Vertical	2	20	60
12.5	Vertical	2	10	60
	C_a = 36%			
3.0	Vertical	2	39	15.6
3.9, 6.0, 7.9	Vertical	2	20	60
11.6	Vertical	2	10	60
	C_a = 14%			
3.9	Vertical	2	20 or 40	60
11.6	Vertical	2	10 or 20	60

pixels was acquired of the flow, and subsequently converted to 8-bit images, over a total image acquisition time $\mathcal{T}_T$ (Table III).

A sequence of 100 images of the vertical central x-z plane at $y = 0$ was also obtained at a lower magnification of 0.40 at $\tau = 2$ ms and $\Delta t = 39$ ms. These images were averaged over $\mathcal{T}_T = 3.9$ s to obtain particle pathline visualizations of the flow, and the contrast and brightness of the average image adjusted to bring out the flow features as required. Almost all (with the exception of a small sliver at x = [2.41 cm:2.44 cm] in the center) of the entire vertical central plane of the flow was visualized in four views, each with a vertical (z) extent of 0.91 cm.

C. Particle-image velocimetry processing

The location of the free surface in the x-z views, corresponding to a bright band (with a typical z-extent of 30 pixels due to light sheet reflections), was considered to be the lower edge of this band. Canny edge detection[20] was used to detect this lower edge from an average of the first 200 images in the sequence, and the images were only processed with an in-house 2D-2C PIV code (implemented in Matlab R2010a®) from $z = 0$ to this lower edge. The "standard" PIV processing procedures used for the horizontal views and much of the vertical central plane (with the exceptions discussed later) to determine the two in-plane velocity components in the liquid entailed direct cross-correlation of 64 (x) × 32 (y) pixels (0.06 cm × 0.03 cm) interrogation windows using a window shift[21] determined from the first 100 image pairs. A Gaussian curve-fit was used to interpolate the location of the correlation peak, and hence the average particle displacement. Any displacement with a correlation peak-to-noise ratio less than 1.2 were considered to be incorrect "outlier" vectors;[22] a standard median filter-based criterion was also used to identify outlier vectors.[23] All outliers were replaced with vectors estimated from their 8 nearest neighbors by bilinear interpolation. Displacements were determined with a 50% overlap between adjacent interrogation windows at a spatial resolution 0.03 cm along x and 0.015 cm along y.

Determining the velocity field in this flow, with its curved meniscus (liquid-vapor interface) near the heated and cooled ends and regions of high shear, also entails some specialized PIV processing approaches, as detailed in Li and Yoda.[24] In all cases, the particle displacements were

divided by Δt to determine the in-plane velocity components. The average and standard deviation of these PIV data were calculated over all 200 realizations. Finally, the velocity vectors obtained over all of these regions and the separate views were combined to create a composite vector plot showing the in-plane velocity components over a single plane.

III. RESULTS

A. Convection at C_a = 96%

For buoyancy-thermocapillary convection where the relative concentration of air in the vapor space above the liquid $C_a = 96\%$ at $p = 101$ kPa (i.e., at ambient conditions), the major flow structures in the central vertical (x–z) plane of the flow are rolls with a counterclockwise rotation (when viewed with the heated end on the right end, and the cooled end on the left end, of the liquid layer), i.e., a positive ω_y. At the lowest applied temperature difference $\Delta T = 0.9\,^{\circ}$C, two rolls are observed, consisting of a "small" roll with a horizontal (x) extent comparable to the depth of the liquid layer next to the heated end and a "large" roll occupying the rest of the flow. Following previous studies, this state is defined to be steady unicellular flow (SUF).[8] As ΔT increases, the large roll "splits," and more small rolls with an x-extent comparable to the depth of the liquid layer form near the heated end; the formation of the first such roll is shown in Figure 3 at $\Delta T = 1.9\,^{\circ}$C. We call this state partial multicellular flow (PMC). As ΔT increases further, the small rolls spread across the test cell towards the cold end, until there are a maximum of nine rolls occupying the entire test cell at $\Delta T = 3.0\,^{\circ}$C, which is defined here as the onset of steady multicellular flow (SMC).[8] The average x-dimension of the five rolls in the central section of the flow, taken to be the spatial wavelength of the rolls, $\lambda_x = 0.57$ cm.

As ΔT is increased further, the number of the rolls decreases (and their wavelength increases). Figure 4 shows a particle pathline visualization of the entire liquid layer (except for the central portion at $0.49 \le x/L \le 0.51$) typical of SMC at $\Delta T = 3.8\,^{\circ}$C ($T_h = 22.2\,^{\circ}$C, $T_c = 18.4\,^{\circ}$C), with a total of eight rolls spanning the entire x-extent of the test cell. The period, or x-dimension, of the rolls decreases slightly towards the heated end.

Figure 5 shows the average liquid-phase velocity field in the central x–z plane of the flow at $y = 0$ near the heated end ($0 \le x/L \le 0.12$) [right] and the cooled end ($0.88 \le x/L \le 1$) [left] of the test cell for the same SMC flow at $\Delta T = 3.8\,^{\circ}$C. As expected, the interfacial flow in the liquid is driven by thermocapillary stresses away from the heated end, i.e., towards the cooled end (buoyancy effects are relatively minor for the $Bo_D < 1$ considered here). Near the bottom, the flow reverses direction, going from the cooled end towards the hot end. There are, however, stagnation points

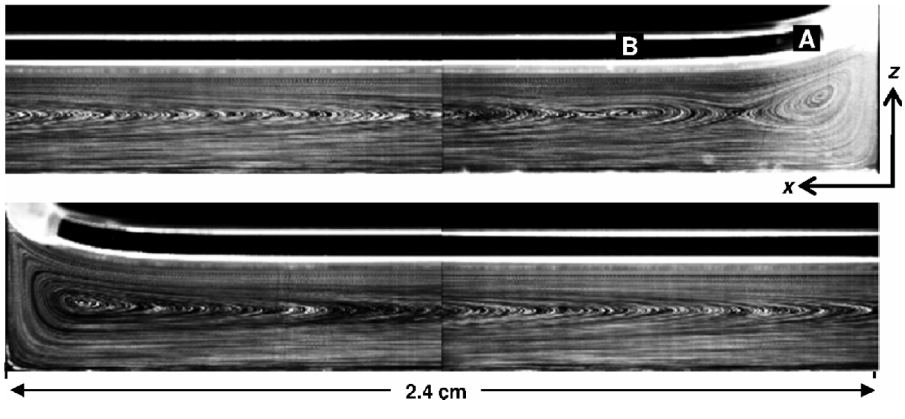

FIG. 3. Particle pathline visualization of PMC flow in a liquid layer with an estimated average layer depth $\bar{h} = 0.266$ cm in the central vertical (x-z) plane at an estimated interfacial Marangoni number $Ma_i = 320$ [$\Delta T = 1.9\,^{\circ}$C], for $0 \le x/L \le 0.49$ next to the heated end [top] and $0.51 \le x/L \le 1$ next to the cooled end [bottom], showing all but a small portion of the center of the liquid layer. Two rolls, labeled A and B, where B is much less evident than A, are visible next to the heated end [top] on the right. Note that the axes shown here and in the subsequent figures only denote the coordinate directions.

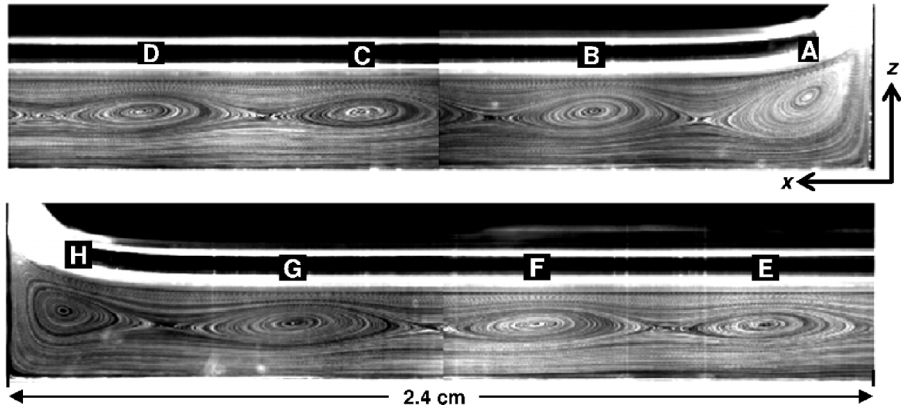

FIG. 4. Particle pathline visualization of SMC flow in the central vertical (x-z) plane of a $\bar{h} = 0.260$ cm liquid layer at an estimated $Ma_i = 510[\Delta T = 3.8\,°C]$ over $0 \le x/L \le 0.49$ next to the heated end [top] and $0.51 \le x/L \le 1$ next to the cooled end [bottom]. Letters are used to label the eight rolls, with roll A immediately adjacent to the heated end [top] on the right and roll H next to the cooled end [bottom] on the left.

at $(x/L, z/\bar{h}) \approx (0.1, 0.58)$ and $(0.9, 0.62)$ near the heated and cooled ends, respectively, which correspond to the ends of the left-/rightmost convection rolls observed in Figure 4. Note that only the in-plane (i.e., x and z) velocity components are measured in these 2D-2C PIV data. This flow is steady, with an average standard deviation in the velocity magnitude calculated over the 200 samples of 1.6% (based on the maximum velocity magnitude) and a maximum of 7% occurring near the contact line in the free surface region.

Figure 6 shows the in-plane velocity components field for the same flow in a horizontal (x-y) plane at $z/\bar{h} = 0.77$ ($z = 0.2$ cm) next to the heated ($0 \le x/L \le 0.25$) [right] and the cooled ($0.75 \le x/L \le 1$) [left] ends of the test cell. This plane is slightly below the free surface in the central portion of the test cell; the depth increases near the heated and cooled ends to a maximum of ~0.4 cm due to capillarity (cf. Fig. 4). As expected, the flow is nearly symmetric about the x-axis, with the flow in the center near $y = 0$ going from the heated to the cooled end, in agreement with the results shown in the vertical plane (Fig. 5) and from the cooled to the heated end near the side walls (i.e., $y/W = \pm 0.5$). We suspect that much of the flow structure evident in this view (i.e., flow reversal near the side walls) is due to the increase in the liquid depth near the walls caused by capillarity, since the contact angle is quite small.

Although the depth of the liquid layer can be estimated from visualizations of the flow, this estimate is flawed because the glare at the liquid-vapor interface and at the bottom of the test cell due to reflected light (cf. Figs. 3 and 4) makes it difficult to precisely determine their actual

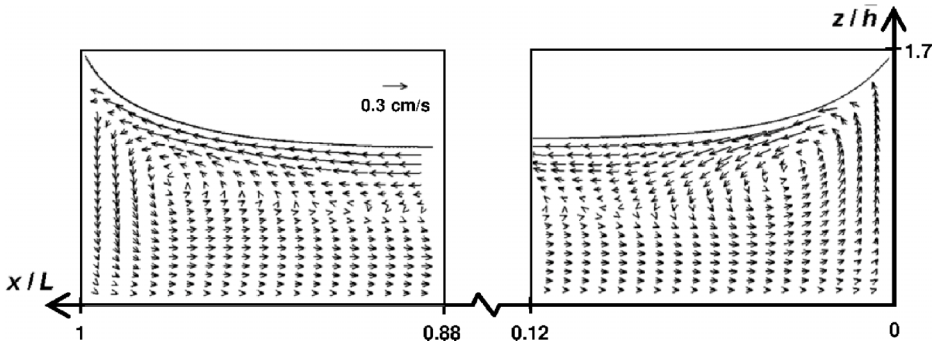

FIG. 5. The velocity field in buoyancy-thermocapillary convection under air in the central vertical (x-z) plane of the flow at $y = 0$ next to the cooled end over $0.88 \le x/L \le 1$ [left], and next to the heated end over $0 \le x/L \le 0.12$ [right] of the test cell for SMC flow at $Ma_i = 510\,[\Delta T = 3.8\,°C]$. The velocity scales are identical for both vector plots, and the maximum velocity magnitudes, which occur just below the free surface, are 0.41 cm/s and 0.51 cm/s near the cooled and heated ends, respectively.

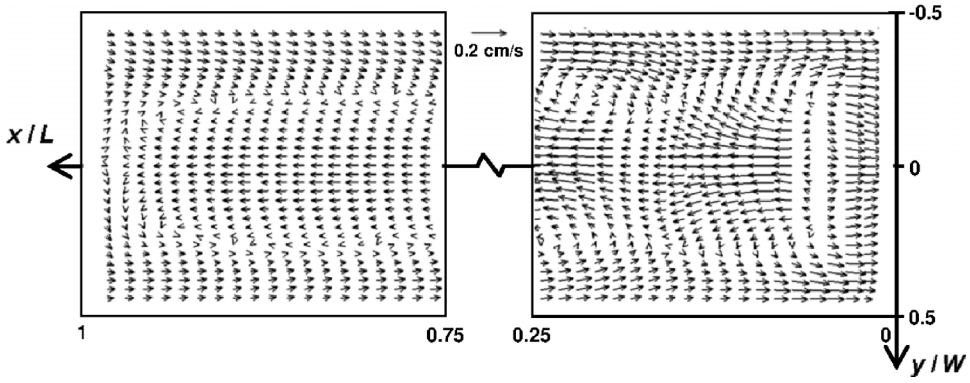

FIG. 6. The in-plane components of the liquid-phase velocity field in SMC flow for $Ma_i = 510$ in a horizontal $(x - y)$ plane at $z/\bar{h} = 0.77$. Both vector plots have the same velocity scale, given in the center. The maximum velocity magnitudes are 0.08 cm/s and 0.19 cm/s near the cooled and heated ends, respectively.

locations. We instead estimated the depth of the liquid layer, as well as the interfacial temperature gradient, by curve-fitting the analytical solution for unidirectional return flow in a laterally infinite layer originally obtained by Birikh[25] and later rederived by Villers and Platten[14] to the measured profile of the horizontal (x) velocity component u over the depth of the liquid layer in the central section of the flow. Following the notation of Ref. 8:

$$\frac{u(z)}{U_s} = \frac{3}{4}\left(\frac{z}{\bar{h}}\right)^2 - \frac{1}{2}\left(\frac{z}{\bar{h}}\right) + Bo_D\left[-\frac{1}{6}\left(\frac{z}{\bar{h}}\right)^3 + \frac{5}{16}\left(\frac{z}{\bar{h}}\right)^2 - \frac{1}{8}\left(\frac{z}{\bar{h}}\right)\right], \tag{4}$$

where $U_s = \gamma\bar{h}\,\tau_i/\mu$ is the thermocapillary velocity scale.

Our use of this analytical solution describing unicellular flow is based on the observation (supported by a number of numerical and experimental studies) that, for volatile liquid layers under ambient conditions and for sufficiently low ΔT, the interfacial temperature gradient τ_i is constant in the central portion of the flow between the thermal boundary layers that form near the temperature-controlled end walls. An extension of Birikh's analytical solution to the flow in the gas phase shows that the magnitude of the gradient is controlled by diffusion of vapor through air.[26] At higher ΔT, when convection rolls appear, the advection of heat in the liquid layer causes modulation of the interfacial temperature about the linear profile (see, for example, Fig. 10(a) of Riley and Neitzel[8]). Numerical simulations performed by our group[27] confirm that the average slope $\bar{\tau}_i$ remains well-defined well above onset of multicellular convection and can be used to describe the average temperature gradient inside the entire liquid layer. Furthermore, a number of linear stability analyses[11,28,29] show that the flow in the liquid can be described by a sinusoidal perturbation in x about (4). The velocity profile averaged along the x direction should therefore still be described by this analytical solution at ΔT even somewhat above the onset of the multicellular state.

These observations enable us to estimate both the average liquid layer thickness $\bar{h}$ and the average interfacial temperature gradient $\bar{\tau}_i$ by comparing the spatially averaged horizontal velocity profiles with the analytical solution (4) even for the flows studied here which are not, strictly speaking, unidirectional. For instance, for the flows shown in Figures 3 and 4, the vertical (z) velocity component w does not vanish due to the presence of convection rolls in the liquid layer. We obtained the mean velocity profile $\bar{u}(z)$ by spatially averaging the horizontal component u over $0.37 \le x/L \le 0.62$. The two vertical locations in the liquid layer where $\bar{u} = 0$, corresponding to the z-coordinates of the bottom of the test cell and the location in the bulk of the layer where flow reversal occurs, were determined by linear interpolation, and the roots of Eq. (4) were determined numerically to estimate $\bar{h}$ and the dynamic Bond number Bo_D. Finally, $\bar{\tau}_i$ was determined from the curve-fit of $\bar{u}(z)$ to Eq. (4) that gave the minimum rms error, and the interfacial Marangoni number Ma_i was calculated based on $\bar{\tau}_i$ and $\bar{h}$.

Figure 7 shows the curve-fits to the average measured nondimensional velocity profiles, and compares them to the analytical solution (solid line) given in Eq. (4) based on the average Bond

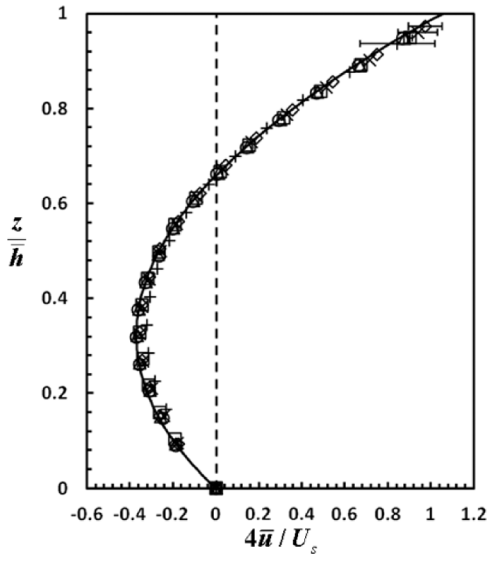

FIG. 7. Spatially averaged profiles of the normalized x-velocity component $4\bar{u}/U_s$ in the liquid layer as a function of the depth normalized by the estimated average liquid layer depth $z/\bar{h}$ for the flows in the SUF, PMC, and SMC states at $Ma_i = 170$ [$\Delta T = 0.9\,^{\circ}$C] (○), 260 [1.4 °C] (△), 320 [1.9 °C] (□), 430 [3.0 °C] (◇), 510 [3.8 °C] (×), and 750 (6.5 °C) (+). The solid curve is the analytical solution for the velocity profile obtained by evaluating Eq. (4) at $Bo_D = 0.69$.

number of 0.69 for all the cases in the SUF, PMC, and SMC states. The good agreement between the spatially averaged velocity data and the analytical solution suggests this procedure can be successfully used to estimate $\bar{h}$ and $\bar{\tau}_i$. The error bars representing the maximum standard deviation in the velocity data are plotted only for the cases in the SMC state (i.e., $Ma_i = 430$, 510, and 750), where the velocity data are averaged over multiple cells, resulting in significant spatial variations in u (cf. Fig. 4). The maximum standard deviations normalized by the velocity at the free surface for $Ma_i = 430$, 510, and 750 are 8.1%, 9.4%, and 18.4%, respectively, while the average standard deviations over the depth are 2.5%, 3.3%, and 9.8%, respectively. The maximum standard deviations for all the SUF and PMC cases are less than 3%, or smaller than the size of the symbols.

Table IV summarizes the flow states and parameters obtained from this curve-fitting procedure for all the experimental cases studied. For convection at $C_a = 96\%$, these estimates suggest that the onset of PMC occurs at $Ma_i = 320$, and the onset of SMC occurs at $Ma_i = 430$, with the nondimensional wavelength of $\lambda_x/\bar{h} \approx 2.2$. The table also gives the velocity at the interface $u(\bar{h})$ based on Eq. (4). Note that Ma_L is calculated based on $\bar{h} = 0.26$ cm. For comparison, this table also includes a limited set of estimates of the interfacial temperature gradient $\tau_{exp} = \Delta T_i/\ell$ based on the temperature difference measured by the thermistors inserted below the free surface ΔT_i and the spacing between these thermistors $\ell = 3.95$ cm. These thermistor readings are, however, unlikely to provide a reliable estimate of the interfacial temperature gradient because of the difficulties in accurately positioning the thermistor beads with respect to the free surface, the deviations from linearity in the interfacial temperature profile near the walls (due to thermal boundary layers), and the large temperature gradient in the vertical direction.

As ΔT continues to increase, the flow remains steady and the number of rolls decreases, with six rolls observed at $Ma_i = 750$ ($\Delta T = 6.5\,^{\circ}$C) (results not shown). For higher values of ΔT, however, the flow starts to become unsteady, as can be seen in the comparison of particle pathline visualizations shown in Figure 8 of a single roll over a quarter of the test cell ($0.51 \le x/L \le 0.75$) over $\mathcal{T}_T = 3.9$ s at $\Delta T = 6.5\,^{\circ}$C (a) and 7.8 °C (b). This unsteady flow was termed an oscillating multicellular flow (OMC),[8] and PIV results (not shown) give a standard deviation in the velocity magnitude of 10% (of the maximum velocity magnitude). Note that this may actually be an underestimate of the fluctuations, since these PIV data may not temporally resolve the flow in the OMC state.

TABLE IV. Summary of experimental parameters and the estimates of Marangoni and Bond numbers based on the curve-fit to Eq. (4).

ΔT (°C)	Ma_L	τ_{exp} (°C/cm)	$\bar{\tau}_i$ (°C/cm)	$\bar{h}$ (cm)	$u(\bar{h})$ (cm/s)	Ma_i	Bo_D	State
			C_a = 96%					
0.9	290		0.11	0.263	0.13	170	0.76	SUF
1.4	450		0.17	0.263	0.20	260	0.76	SUF
1.9	620		0.20	0.266	0.24	320	0.78	PMC
3.0	910		0.29	0.256	0.34	430	0.72	SMC
3.8	1190	0.38	0.33	0.260	0.39	510	0.74	SMC
6.5	1880		0.53	0.249	0.60	750	0.68	SMC
7.8	2260		0.56	0.250	0.63	780	0.69	OMC
11.5	3590	0.81	0.66	0.260	0.77	990	0.74	OMC
			C_a = 57%					
2.8	750		0.28	0.240	0.30	370	0.63	SUF
3.9	1050		0.37	0.241	0.39	480	0.64	PMC
6.8	1790		0.52	0.238	0.56	670	0.62	PMC
9.8	2600		0.64	0.239	0.69	830	0.63	SMC
12.5	2960		0.73	0.226	0.73	870	0.56	SMC
			C_a = 36%					
3	870		0.31	0.249	0.35	440	0.68	SUF
3.9	1090		0.37	0.245	0.41	500	0.66	SUF
6	1690		0.50	0.246	0.55	680	0.67	PMC
7.9	2150		0.58	0.242	0.63	770	0.65	PMC
11.6	2910		0.73	0.233	0.75	880	0.59	PMC
			C_a = 14%					
3.9	1340	0.38	0.38	0.273	0.47	630	0.82	SUF
11.6	3420	0.71	0.72	0.252	0.82	1040	0.70	PMC

Figure 9 shows a sequence of "snapshots" of velocity field $\Delta T = 11.5\,°C$ ($T_h = 28.1\,°C$, $T_c = 16.6\,°C$) overlaid with the out-of-plane (y) component of the vorticity ω_y calculated from the PIV data in the vertical (x-z) central plane at $y = 0$ next to the heated end ($0 \le x/L \le 0.25$). Here, ω_y was determined using PIV results that were obtained as discussed previously with an overlap

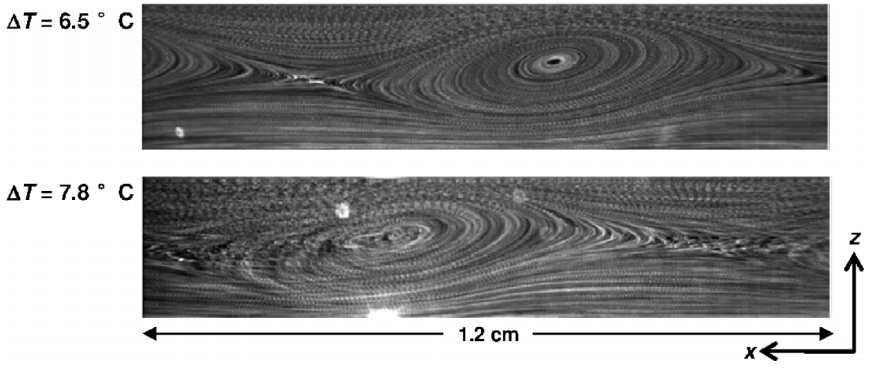

FIG. 8. Magnified particle pathline visualizations of the flow over about a quarter of the test cell ($0.51 \le x/L \le 0.75$) in the central vertical (x-z) plane at $Ma_i = 750$ [$\Delta T = 6.5\,°C$] [top] and $Ma_i = 780$ ($\Delta T = 7.8\,°C$) [bottom]. Note the blurring of the pathlines at the higher Ma_i.

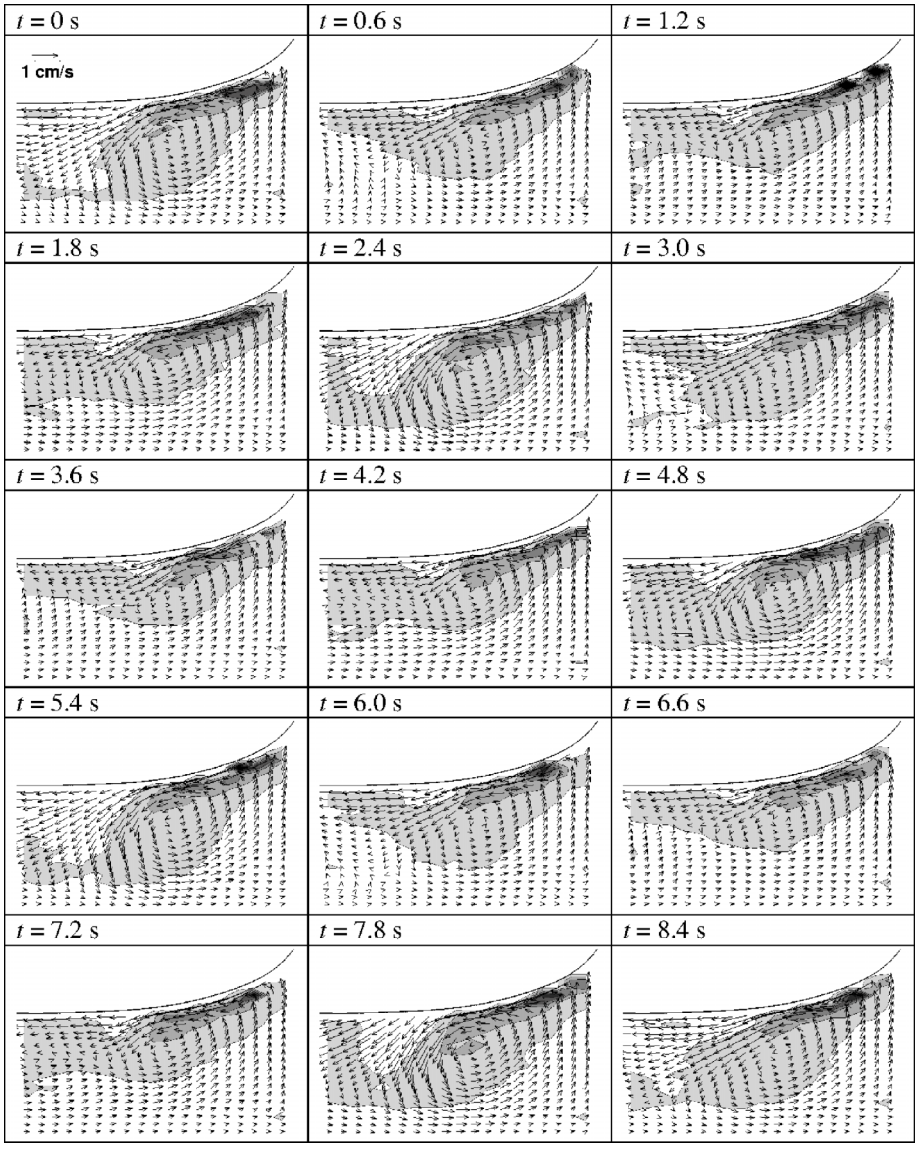

FIG. 9. Time sequence showing the y-component of the vorticity every 0.6 s calculated from the PIV data next to the heated end over $0 \le x/L \le 0.12$ at an estimated $Ma_{\mathrm{i}} = 990$ [$\Delta T = 11.5\,^{\circ}\mathrm{C}$] and $Bo_{\mathrm{D}} = 0.74$. The shading denotes the vorticity, with the light gray shade representing $3\ \mathrm{s}^{-1} \le \omega_y \le 19.2\ \mathrm{s}^{-1}$, the medium gray shade representing $19.2\ \mathrm{s}^{-1} \le \omega_y \le 35.4\ \mathrm{s}^{-1}$, and the dark grey shade representing $\omega_y > 35.4\ \mathrm{s}^{-1}$. These vorticity contour plots overlay the PIV velocity data, which have the same velocity scale (given in the image at $t = 0$) with a maximum speed of 2.12 cm/s at $t = 7.8$ s.

of 75% between adjacent interrogation windows from the circulation, calculated using filtered second-order differencing of the eight nearest neighbor velocities.[30]

In this sequence, the roll next to the heated end (cf. roll A in Fig. 4) appears to oscillate, while the next roll (cf. roll B in Fig. 4) appears to travel towards the cooled end. In these plots, the free surface is denoted by the uppermost curved line, and the in-plane velocity field, shown by the arrows, is overlaid with a contour plot of ω_y thresholded so that only values of $\omega_y > 3\ \mathrm{s}^{-1}$ (i.e., regions with significant counterclockwise rotation) are shown. The sequence of images starting at $t = 0$ shows the roll next to the heated end; this roll grows in both horizontal and vertical extent with the region where $\omega_y > 3\ \mathrm{s}^{-1}$ reaching its maximum depth around $t = 2.4$ s, where we observe a "pocket" of high-speed, but low-vorticity fluid near the liquid-vapor interface. This pocket is much smaller by $t = 3.0$ s, and the vertical extent of the roll decreases with time until we see a structure

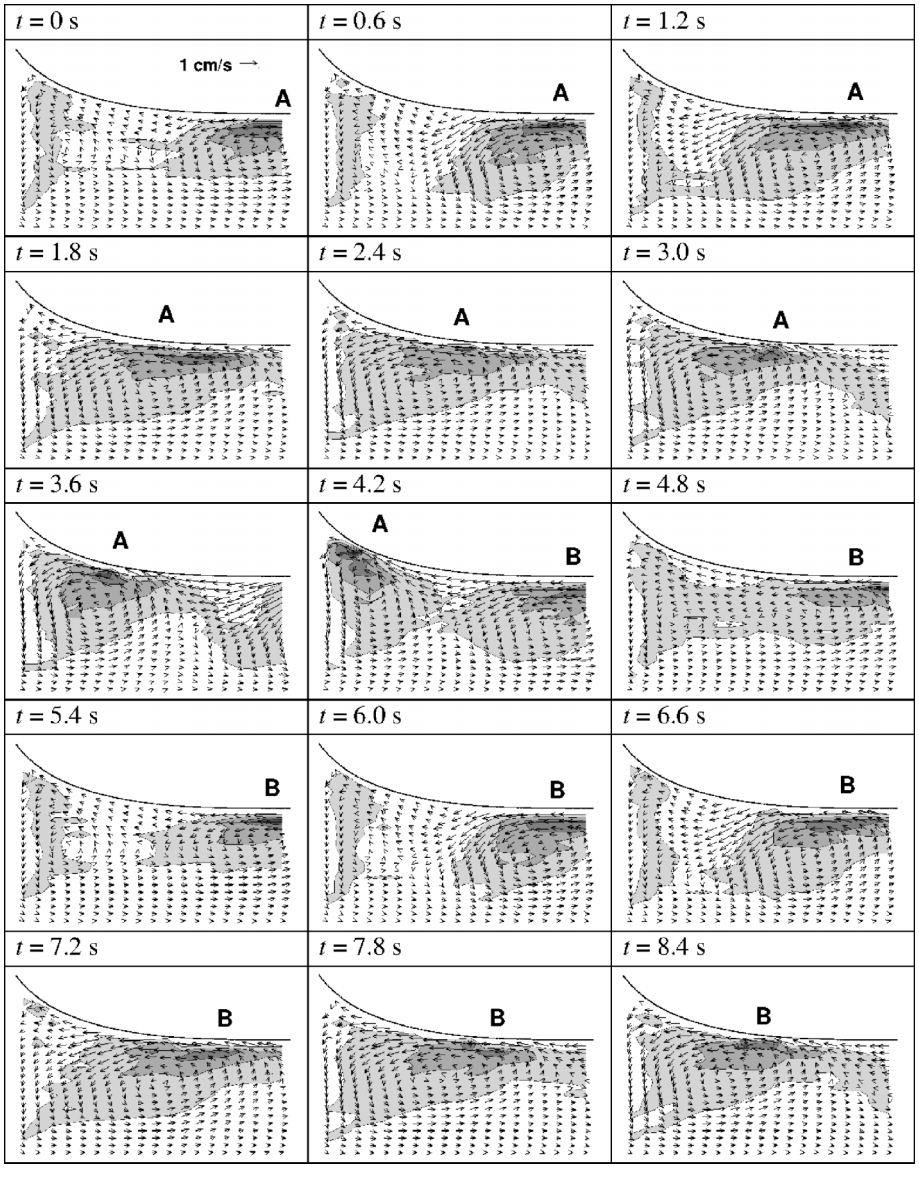

FIG. 10. Similar to Fig. 9, but for the flow next to the cooled end over $0.88 \leq x/L \leq 1$. Each roll is labeled by a letter above its region of highest ω_y. The shading denotes the vorticity, with the light gray shade representing $3\ s^{-1} \leq \omega_y \leq 10.8\ s^{-1}$, the medium gray shade representing $10.8\ s^{-1} \leq \omega_y. \leq 18.6\ s^{-1}$, and the dark grey shade representing $\omega_y > 18.6\ s^{-1}$. The out-of-plane vorticity component overlays the PIV velocity data, which have the same scale (given in the inset of the image at $t = 0$); the maximum speed is 1.13 cm/s at $t = 6.0$ s.

at $t = 5.4$ s very similar to that at the beginning of this sequence, or $t = 0$. Although not shown here, this oscillation in the height of this roll, represented here by the region where $\omega_y > 3\ s^{-1}$, is observed over several periods during the total PIV data acquisition time of 60 s.

Figure 10 shows a similar sequence of ω_y"snapshots" in the vertical (x-z) central plane at $y = 0$ next to the cooled end ($0.75 \leq x/L \leq 1$) for the same flow. No oscillatory behavior is observed near the cooled end, with rolls instead traveling to the left, or towards the cooled end. Starting at $t = 0$, a roll (A), represented here by the region where $\omega_y > 3\ s^{-1}$, enters on the right side and travels towards the cooled end, becoming more elongated and reaching the cooled wall by $t = 4.2$ s, when the second roll in the pair (B) enters on the right side. Roll B then travels towards the cooled end, with the high-vorticity "core" of roll A no longer evident by $t = 4.8$ s, and by $t = 6.6$ s, the position of roll B looks much like that of roll A at $t = 1.2$ s. This sequence suggests that the

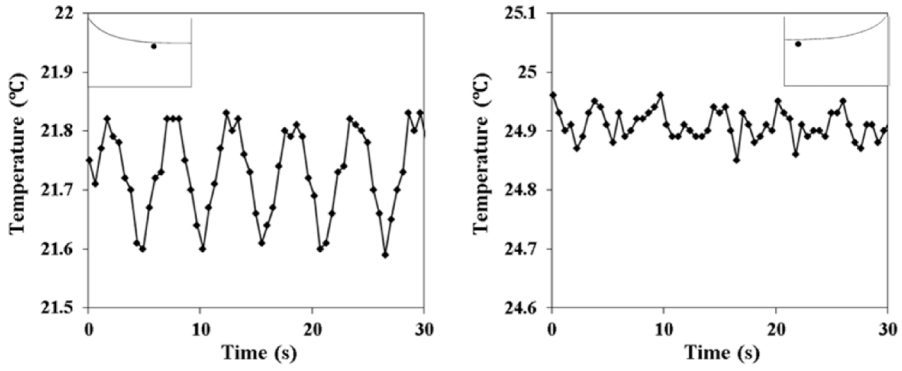

FIG. 11. The variation in temperature over time near the cooled [left] and heated [right] ends for the flow shown in Figures 9 and 10 at $Ma_i = 990$ [$\Delta T = 11.5\,°C$]. The actual temperature readings are given by the symbols, and the lines connecting the datapoints are provided as a visual guide. Note that the extent of the vertical axis (0.5 °C) is the same for both plots. The insets in the upper outer corners of each plot show the position of the thermistors as black dots with respect to the cooled and heated ends and the liquid-vapor interface.

interval between successive rolls, based on when they enter on the right side of this field of view, is about 5.4 s, in agreement with the period observed in the sequence near the heated end in Fig. 9.

Figure 11 shows interfacial temperature readings over 30 s from glass-sealed thermistors (Honeywell 111-103EAJ-H01, with bead diameter 0.036 cm and accuracy of 0.1 °C) 0.028 cm below the interface near the cooled [left] and heated [right] ends at $x/L \approx 0.11$ and 0.92, respectively, from another realization of the flow under the same conditions. Unfortunately, difficulties in reproducibly locating the thermistors, which were inserted through the two test cell ports on flexible wires >7 cm in length before evacuating the test cell (and hence before knowing the location of the free surface), made it impractical to do more than monitor temperatures near the interface with this approach.

Near the cooled end ($x/L = 0.92$, cf. inset), the interfacial temperature has marked oscillations with a peak-to-peak amplitude of about 0.3 °C. An FFT of these temperature data gives a strong peak at a frequency of 0.177 Hz, corresponding to an oscillation period of 5.6 s, in agreement with the observations near the cooled end in Figure 10. The temperature near the heated end ($x/L = 0.11$, cf. inset) also appears to have weak fluctuations, but their amplitude is comparable to the measurement accuracy, and the fluctuations appear to be less periodic than those observed near the cooled end although an FFT of these data also has a distinct peak at a frequency of 0.177 Hz, in agreement with the observations from Figure 9.

The strongly time-oscillatory behavior observed in the temperature here at a single point near the free surface in Figure 11 [left] is qualitatively similar to that observed in the single-point laser-Doppler velocimetry (LDV) measurements of Refs. 9 and 14 and qualitatively similar oscillatory behavior is also observed in the velocities measured using PIV (admittedly obtained at much lower sampling frequencies and at significantly coarser spatial resolution than the LDV measurements) at the same location, as shown in Figure 12.

Surprisingly, the curve-fitting procedure used to estimate $\bar{h}$ and $\bar{\tau}_i$ for the steady flow states appears to work reasonably well for the spatially and temporally averaged velocity data in the OMC state as well, as shown in Figure 13. Estimates of $\bar{h}$, $\bar{\tau}_i$, Ma_i, and Bo_D are therefore also given in Table IV (for $C_a = 96\%$). Based on these estimates of the interfacial Marangoni number, the onset of time-dependent flow appears to occur at a critical Ma_i between 750 and 780, and $\bar{h} = 0.260$ cm. These estimates also give $Ma_i = 990$ and $Bo_D = 0.74$ for the flow shown in Figures 9–12.

B. Convection at C_a = 57% and 36%

Buoyancy-thermocapillary convection was also studied under a vapor space containing 57% and 36% air under otherwise similar conditions. Flow visualizations (not shown here) for these "intermediate" air concentrations over a similar range of ΔT (Table IV) show that reducing C_a (and the pressure) in the vapor space affects the stability of the flow and increases the critical Marangoni

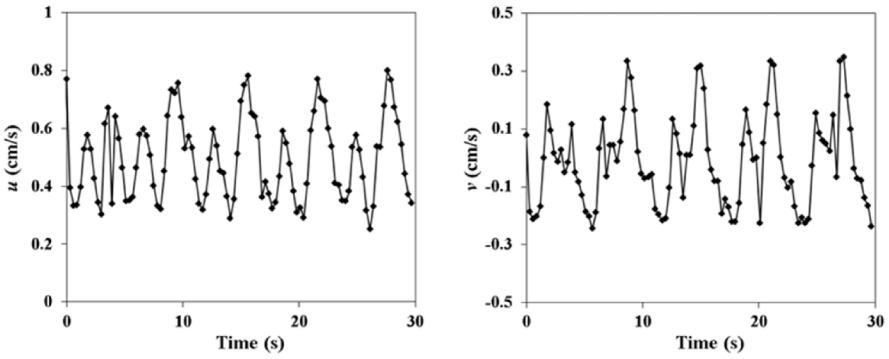

FIG. 12. Graphs showing u [left] and v [right], the velocity components along x and y, respectively, as a function of time for the same flow at $Ma_i = 990$ [$\Delta T = 11.5\,^{\circ}\mathrm{C}$] just below the liquid-vapor interface at $x/L = 0.92$, corresponding to the location of the temperature data given in Figure 11 [left]. Again, the actual velocities are given by the symbols, and the lines are a visual guide.

numbers for the onset of different flow states. At $C_a = 57\%$, the flow transitions from the SUF to PMC to SMC states as ΔT increases; the OMC state is not observed at even the highest ΔT value of 12.5 °C ($Ma_i = 870$). At $C_a = 36\%$, the flow only transitions from the SUF to PMC states, and neither SMC nor OMC flow is observed for $\Delta T \le 11.6\,^{\circ}\mathrm{C}$ ($Ma_i = 880$).

Figures 14(a) and 14(b) compare $\bar{u}(z)$ (i.e., the velocity component spatially averaged over $0.37 \le x/L \le 0.62$) with that given by Eq. (4) at the average $Bo_D = 0.69$ for $C_a = 57\%$ and 36%, respectively. The experimentally measured profiles and the analytical solution are also in good agreement at these lower C_a, and estimates of $\bar{h}$, $\bar{\tau}_i$, Ma_i, and Bo_D are also given in Table IV. The error bars again represent the maximum standard deviations in the spatially averaged velocity, which occurs near the free surface. For $C_a = 57\%$, the maximum standard deviations normalized by the velocity at the free surface at $Ma_i = 670$, 830, and 870 are 5.9%, 7.6%, and 12.2%, respectively (Fig. 14(a)), with average standard deviations of 2.9%, 4.2%, and 8.1%, respectively. For $C_a = 36\%$, the maximum and average standard deviations at $Ma_i = 880$ are 3.4% and 1.9%, respectively. For all other cases, the maximum standard deviations are again smaller than the symbols.

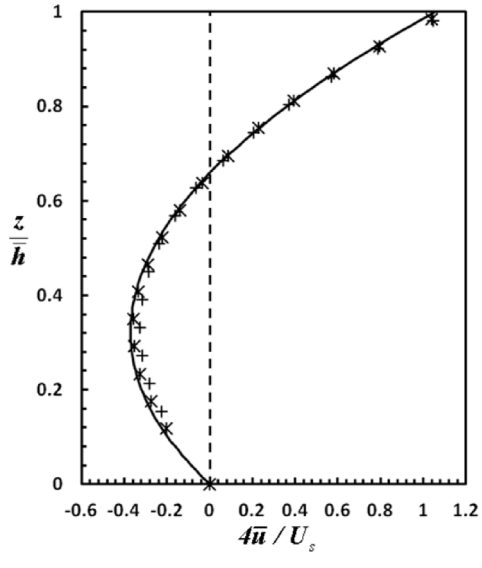

FIG. 13. Similar to Figure 7, but for the OMC cases at $Ma_i = 780$ [$\Delta T = 7.8\,^{\circ}\mathrm{C}$] (+) and 990 [11.5 °C] (∗).

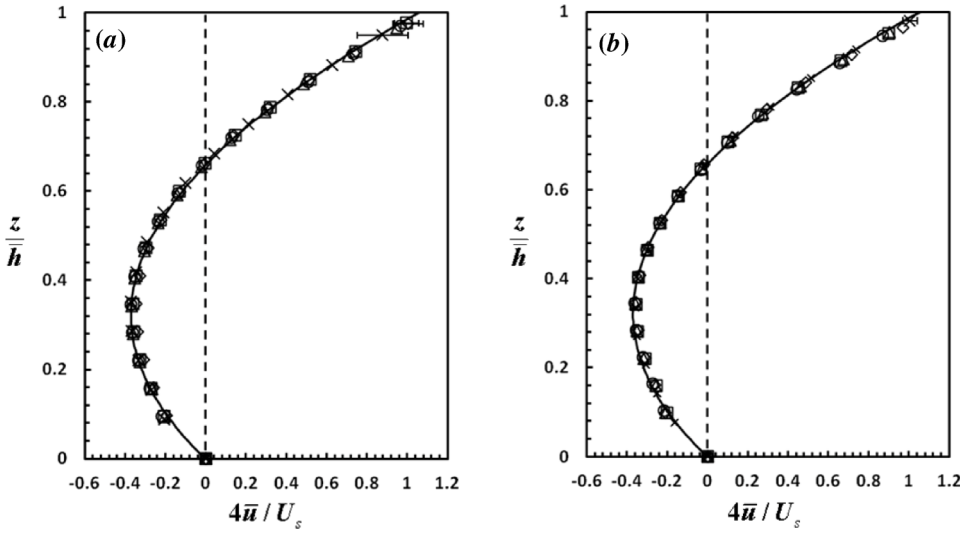

FIG. 14. Similar to Figure 7, but for the C_a = 57% case (a) at Ma_i = 370 [ΔT = 2.8 °C] (○), 480 [3.9 °C] (△), 670 [6.8 °C] (□), 830 [9.8 °C] (◇), and 870 [12.5 °C] (×); and C_a = 36% (b) at Ma_i = 440 [ΔT = 3.0 °C] (○), 500 [3.9 °C] (△), 680 [6.0 °C] (□), 770 [7.9 °C] (◇), and 880 [11.6 °C] (×).

C. Convection at C_a = 14%

The lowest noncondensables fraction that could be achieved in these experiments was about 14%. Figure 15 shows a particle pathline visualization of buoyancy-thermocapillary convection at C_a = 14% over the entire liquid layer (except for $0.49 \le x/L \le 0.51$) at ΔT = 3.9 °C. The flow, with a small roll next to the heated end and a large roll occupying the rest of the liquid layer is typical of SUF. Figure 16 shows the average liquid-phase velocity field in the central vertical (x–z) plane of the flow at $y = 0$ near the heated end ($0 \le x/L \le 0.12$) [right], and near the cooled end ($0.88 \le x/L \le 1$) [left] of the test cell for this case. At the maximum temperature difference studied, ΔT = 11.6 °C, the flow is still in the PMC state, with the large roll having only "split" off a single roll, B (Fig. 17), suggesting that the flow is just past the SUF/PMC threshold.

Figure 18 compares $\bar{u}(z)$ with the analytical solution at Bo_D = 0.69. The average velocity profiles and the analytical solution are in good agreement, as was the case at higher C_a. Estimates for flow parameters obtained using the procedure described earlier are, therefore, also included in Table IV for C_a = 14%. No error bars are shown on this plot because the maximum and average standard deviations in the velocity data are smaller than the symbols in all cases.

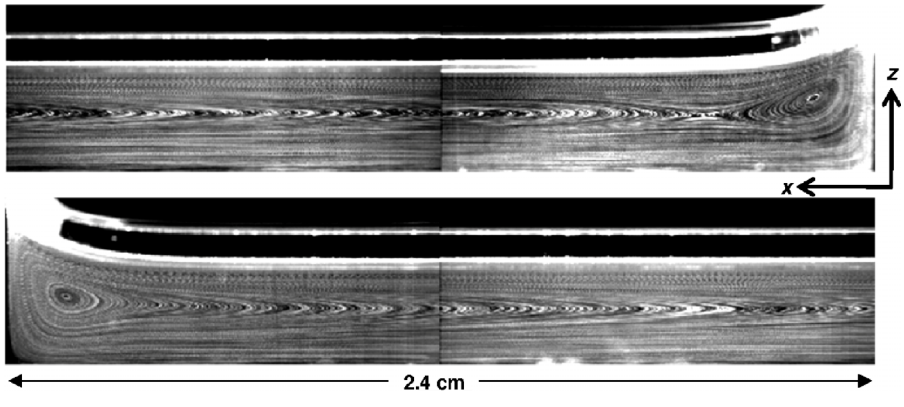

FIG. 15. Particle pathline visualization of the flow in the central vertical (x-z) plane of a liquid layer with an estimated average depth $\bar{h}$ = 0.263 cm at an estimated Ma_i = 630 [ΔT = 3.9 °C] and Bo_D = 0.82 for $0 \le x/L \le 0.49$ next to the heated end [top] and $0.51 \le x/L \le 1$ next to the cooled end [bottom].

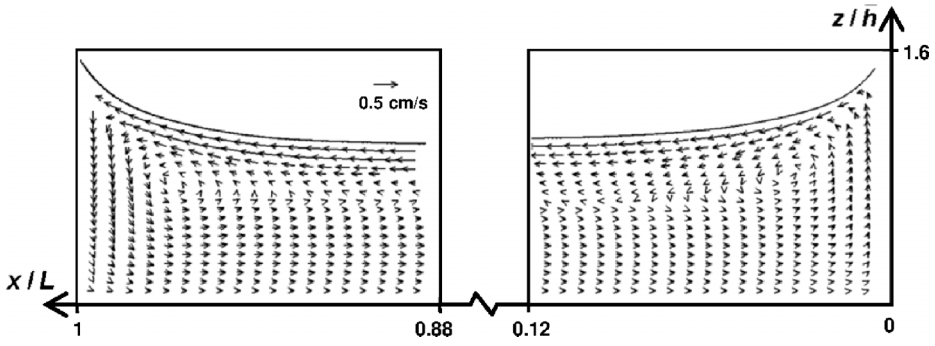

FIG. 16. The velocity field for the same flow in the central vertical (x-z) plane next to the cooled end over $0.88 \le x/L \le 1$ [left] and next to the heated end over $0 \le x/L \le 0.12$ [left]. The maximum velocity magnitudes, which occur just below the free surface, are 0.61 cm/s and 0.43 cm/s near the cooled and heated ends, respectively.

IV. DISCUSSION

A. Convection at C_a = 96%

Our results for convection under a vapor space dominated by air at $p = 101$ kPa are in qualitative agreement with previous experimental studies of buoyancy-thermocapillary convection at ambient conditions and $\Gamma_y < 6$ where transverse confinement is significant (summarized in Ref. 10). To our knowledge, the only experimental studies of convection in nonisothermal liquid layers where thermocapillarity, buoyancy, and transverse confinement are significant are Refs. 9, 13, 14, and 17. The earliest study was that by Villers and Platten,[14] who measured velocity profiles in $h = 0.175 - 1.425$ cm deep acetone ($Pr = 4.2$) layers of dimensions $L = 3$ cm and $W = 1$ cm and compared their results with numerical simulations. They reported that the flow transitioned from a unicellular steady state to a multicellular steady state to a time-dependent flow as the Marangoni number increased. The results presented here clearly follow the same sequence, with the transition from the SUF to PMC states occurring at a critical $Ma_i \approx 320$ for $Bo_D = 0.78$, transition from PMC to SMC states occurring at $Ma_i \approx 430$ for $Bo_D = 0.72$, and the transition from the SMC to OMC states occurring at a Ma_i between 750 and 780 for $Bo_D = 0.69$. Villers and Platten[14] termed the time-dependent flow state at high Marangoni numbers "oscillatory convection" and showed that the variation in the measured x-component of velocity was time-periodic. Their numerical simulations showed that a new vortex is created near the hot wall and then travels about half way to the cold wall, in the direction opposite to that of the hydrothermal waves, after which it dissipates and the process repeats. The authors reported that they "never observed travelling waves with the

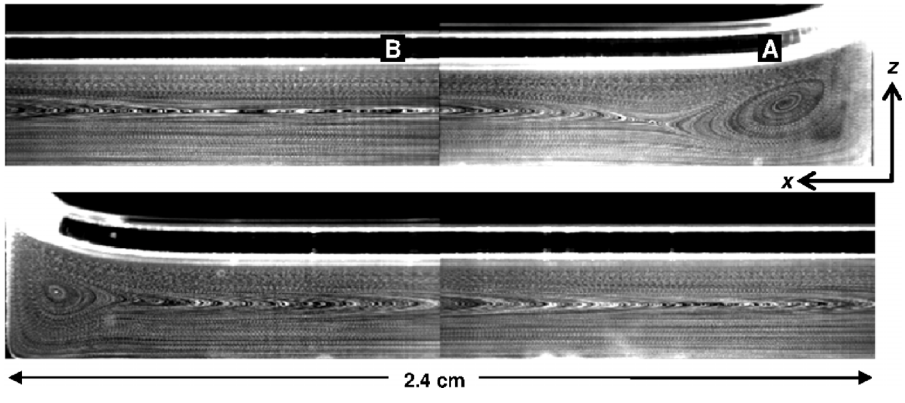

FIG. 17. Particle pathline visualization of the flow in the central vertical (x-z) plane for $C_a = 14\%$ at an estimated $Ma_i = 1040$ [$\Delta T = 11.6$ °C] and $Bo_D = 0.70$, over $0 \le x/L \le 0.49$ next to the heated end [top] and $0.51 \le x/L \le 1$ next to the cooled end [bottom].

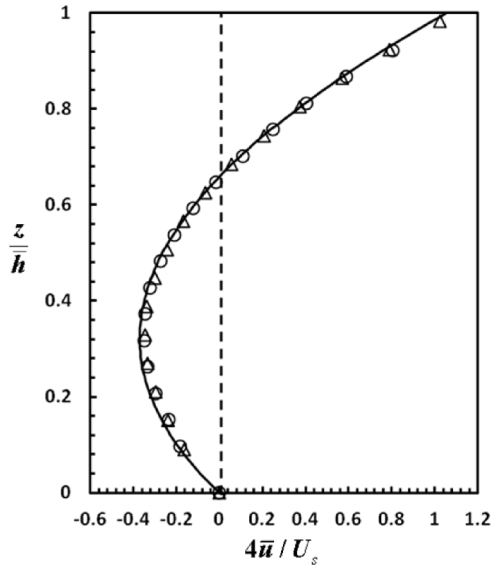

FIG. 18. Nondimensional velocity profiles in the liquid layer $4\bar{u}/U_s$ as a function of $z/\bar{h}$ measured using PIV for $C_a = 14\%$ compared with the analytical solution for $Bo_D = 0.69$ at $Ma_i = 630$ [$\Delta T = 3.9\,°C$] (○) and 1040 [$\Delta T = 11.6\,°C$] (△).

appearance of rolls near one wall and the corresponding disappearance near the opposite wall." Their numerical results are consistent with our observations only near the hot wall. Near the cold wall, however, we find that the waves are travelling towards the cold wall. This difference is likely due to the larger streamwise aspect ratio of the present studies, $\Gamma_x = 20$, *vs.* the $\Gamma_x = 9$ considered by Villers and Platten.[14] Our numerical simulations of a two-sided model performed for $\Gamma_x = 19.8$ produce OMC states that are very similar to the experimental observations near both end walls.[26]

In a subsequent study, De Saedeleer *et al.*[9] also measured velocity profiles in $h = 0.25 - 0.47$ cm deep layers of decane ($Pr = 15$) with $L = 7.4$ cm and $W = 1$ cm, and also reported transition from a steady unicellular flow to steady multicells (which they attributed to confinement) to time-periodic flow as the temperature gradient, and hence Marangoni number, increased. They showed that the horizontal (x) and vertical (z) velocity components had the same period for the time-periodic flow state, but did not further study this flow state because of the limitations of LDV, which "is not very well suited to perform measurements of a rapidly changing velocity pattern" because it measures (usually a single component of) the velocity at a single point.

Garcimartín *et al.*[17] visualized the temperature field using interferometry and the flow using shadowgraphy in $L = 7$ cm, $W = 1$ cm, and $h = 0.2 - 0.35$ cm deep layers of decane and 0.65 and 2.0 cS ($Pr \approx 10$ and 30, respectively) silicone oils. By imaging the entire flow, they showed that the time-dependence was associated with oscillation of the roll nearest to the heated end combined with the adjacent roll traveling towards the cooled end, and noted that similar waves traveling towards the cooled end were also observed in the experiments of Ezersky *et al.*[31] with 5.0 cS silicone oil, albeit in a cylindrical geometry. They suggested that these "waves propagating from the hot side to the cold side" were due to an instability of the thermal boundary layer *along the hot wall*, with the perturbations due to the oscillations of the roll next to the heated end amplified and convected towards the cooled end.

Our PIV results further quantify the phenomena reported by Ref. 17 in terms of the velocity field. The observed period can be compared with the recirculation times for roll A, i.e., the roll immediately adjacent to the heated end, which can be computed by integrating the inverse of the speed along the streamlines of the time-averaged flow reconstructed from the PIV data. We find that the period matches the recirculation time for the streamlines that lie at the periphery of the roll (Figure 19). These streamlines are much closer to the free surface, with a minimum distance of about 0.02 cm, than they are to the hot wall, with a minimum distance of about 0.1 cm. This suggests that the instability is likely driven by the jet of rapidly moving hot fluid at the free surface, rather than the

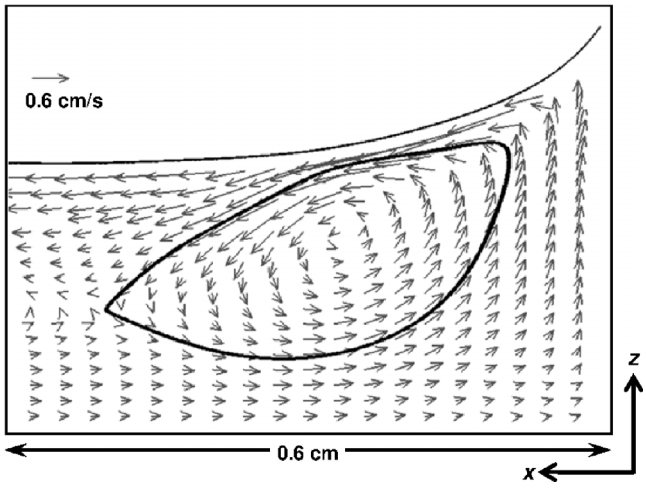

FIG. 19. A streamline calculated from the time-averaged velocity vectors (also shown) of Figure 9 for convection at $C_a = 96\%$ and an estimated $Ma_i = 990$ [$\Delta T = 11.5\,^{\circ}\mathrm{C}$] over $0 \le x/L \le 0.12$ corresponding to the periphery of the counterclockwise roll immediately next to the heated end. The curved line indicates the free surface. The recirculation time for the streamline is estimated to be 5.2 s.

vertical thermal boundary layer forming at the hot wall, as was suggested by Garcimartín *et al*. A more likely mechanism for this instability is due to the momentum transfer between the free surface and the interior of the convection roll. We conjecture that an increase of the temperature gradient τ_i at the free surface near the hot wall leads to an increase in the thermocapillary stresses which accelerate the hot interfacial jet, whose momentum is gradually transferred to the convection roll. The enhanced advection of heat flattens the temperature gradient at the free surface, reducing the thermocapillary stresses, slowing the interfacial hot jet and, subsequently, the recirculation in the convection roll. This eventually leads to an increase of the temperature gradient and a new cycle. Since the extrema in the velocity of the liquid at the free surface and inside the convection roll are out of phase, the cycle can repeat indefinitely, if the time required for the thermal disturbances to travel around the convection roll is the same as the period of the momentum transfer.

While our experimental results are in qualitative agreement with other experimental and numerical studies of buoyancy-thermocapillary convection in the limit of $Bo_D = O(1)$ (i.e., when buoyancy is non-negligible), there are definite quantitative differences. Unfortunately, none of the previous experimental studies have clearly defined the threshold between the SUF and SMC states; as the results presented here show that the transition from unicellular to steady multicellular flow is gradual and involves an intermediate state (PMC), which exists over a reasonably broad range of Ma_i and features between three and eight convection cells that do not fill the entire liquid layer. Transition to SMC eventually takes place at a critical Marangoni number $Ma_i = 430$ (at $Bo_D = 0.72$) when nine convection cells do fill the entire layer.

This is lower than the critical $Ma_i = 482$ found by Riley and Neitzel[8] at $Bo_D = 0.72$. The discrepancy is most likely due to the difference in the Prandtl number of the liquids ($Pr = 9.2$ for HMDS, compared with $Pr = 13.9$ for the higher-viscosity silicone oil used by Riley and Neitzel). As the linear stability analysis of Priede and Gerbeth[29] showed, Ma_i increases with Pr (for Pr above ~1). Another difference between the two experiments is the (transverse) aspect ratio Γ_y, which was much larger for Riley and Neitzel than that studied here although the flow structure was essentially two-dimensional in both studies, so it seems unlikely that transverse confinement would significantly affect either the structure of the flow or its stability.

Unfortunately, there are also remarkably few theoretical studies that can be used for quantitative comparison. While the numerical simulations[14,32,33] suggest, in agreement with experiments, that the unicellular flow transitions to a steady multicellular flow at $Bo_D = O(1)$, their predictions are based on one-sided 2D models which ignore transport in the gas phase as well as phase change and use different values of Bo_D and Pr. Our numerical study (also 2D) finds that the transition from

SUF to PMC for $Bo_D = 0.70$ and $Pr = 9.2$ occurs at Ma_i between 302 and 394, and that from PMC to SMC occurs at Ma_i between 541 and 602.[34]

Numerical simulations also suggest that the critical Ma_i is likely to be quite insensitive to the curvature of the free surface near the end walls. Our numerical results for a wide range of contact angles show the curvature of the free surface near the end walls has a very small effect not only on the heat transfer, but also on the flow regime.[26] On the other hand, the curvature near the side walls (e.g., 3D effects) could play a significant role. Our observations based on sessile drop visualizations suggest that the contact angle of HMDS on fused silica is very small, less than 10°. As a result, the thickness of the liquid layer near the side walls is estimated to be greater by about 40% compared to the average thickness $\bar{h}$, which would effectively double the values of Bo_D and Ma_i.

The theoretical studies which used linear stability analysis for an unbounded liquid layer[11,35] predict transition to an oscillatory instability at all values of Bo_D, with convection rolls traveling from the cold to the hot wall for smaller Bo_D and in the opposite direction for larger Bo_D. Mercier and Normand[28] showed that transition to the SMC state is possible in the presence of a strong vertical heat flux (i.e., non-zero Biot number Bi), which is not the case for our experimental setup. The only (to our knowledge) linear stability study that predicts a transition towards a stationary multicellular state for adiabatic boundary conditions is due to Priede and Gerbeth[29] who argued that the end walls play a very important role. Indeed, in a bounded system (finite Γ_x), disturbances that would be amplified as a result of an oscillatory instability are swept to one of the end walls before they can grow sufficiently to be observed. Their calculations predict the onset of steady multicellular flow to occur at $Ma_i = 540$ for $Bo_D = 0.75$ and $Pr = 13.9$, which is slightly higher than the value found by Riley and Neitzel.[8]

Transition from the SMC to the OMC states in our system occurs at the laboratory Marangoni number $Ma_L \approx 2100$ which is also lower than the value $Ma_L < 3800$ found by Villers and Platten[14] at $Bo_D = 0.7$ in acetone (no estimate of Ma_i is possible since τ_i was not measured in these studies). This discrepancy is likely also be due to differences in Prandtl number (the silicone oil used here has Pr that is more than twice that of acetone, with $Pr = 4.2$).

B. Effect of noncondensables

The present study is, to our knowledge, the first to investigate how changing the relative concentration of noncondensables in the vapor space affects buoyancy-thermocapillary convection. Figure 20 summarizes the flow state observations at $C_a = 14\%$ (*filled black*), 36% (*open black*), 57% (*filled gray*), and 96% (*open gray symbols*) on a $Ma_i - C_a$ flow regime map. Noncondensables

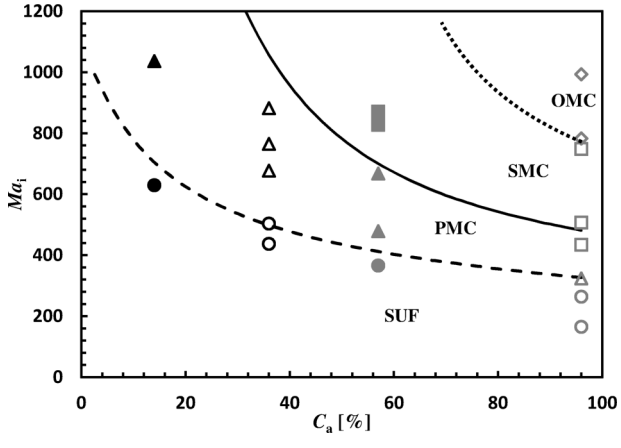

FIG. 20. Flow regime map showing Ma_i as a function of C_a for buoyancy-thermocapillary convection at $C_a = 14\%$ (*filled black*); 36% (*open black*); 57% (*filled grey*); and 96% (*open grey*). The type of symbol denotes the actual flow state: SUF (*circles*); PMC (*triangles*); SMC (*squares*); and OMC (*diamonds*). The thresholds predicted by linear stability are shown as a dashed line (PMC) and solid line (SMC). The dotted line is a sketch of the boundary between SMC and OMC states based on experimental data.

have a very pronounced effect on the stability of the different flow states. As C_a is decreased, all of the transition thresholds increase monotonically. In fact, some of the states disappear completely at lower values of C_a. In particular, unsteady (OMC) flow is only observed at $C_a = 96\%$ here, and SMC flow is only observed at $C_a = 57\%$ and 96%.

These experimental observations are consistent with the results of parallel numerical studies,[26,27,34] which also show that lowering C_a increases the critical Marangoni number for all the transitions. The predicted interfacial flow velocity for the base flow (SUF) is also in reasonable agreement with experimental observations. In the experiments, we find that the flow speeds near the interface and the estimates of τ_i remain essentially independent of C_a over the range from 14% to 96%, which suggests that the thermocapillary stresses remain essentially constant (at a fixed ΔT) until C_a decreases to even lower values. For example, at $\Delta T = 3.8 - 3.9\,^{\circ}\mathrm{C}$ (when the flow is steady in all cases), the velocity at the interface $u(\bar{h})$ varies from 0.39 cm/s to 0.47 m/s, and τ_i varies from 0.33 to 0.38 °C/cm (Table IV). Similarly, the numerical simulations predict that τ_i decreases only slightly (by about 18%) as C_a is reduced from 96% to 16% for $\Delta T = 10\,^{\circ}\mathrm{C}$.[36] As shown in Ref. 27, the interfacial temperature is essentially equal to the saturation temperature, which is a function of the local concentrations of air and vapor. As long as C_a is not too small (at least ~8%, according to Ref. 36), the gradient in the relative concentration of the two components (and hence partial pressure and saturation temperature) persists, and τ_i remains essentially independent of C_a, in agreement with these experimental results.

The observation that the critical Ma_i for transition to the PMC and SMC states increases as C_a decreases is also consistent with the related experimental study by Barthes *et al.*,[37] who explored the dynamics of bubbles forming in liquids with and without dissolved gases and found that the bubbles grew steadily in degassed liquids but developed oscillations in liquids with dissolved gases. Although the study did not report the relative fraction of noncondensables, the oscillations were attributed to the enhancement of thermocapillary stresses by noncondensable gases inside the bubble; these stresses, of course, effectively disappear in the absence of noncondensables.

In order to gain a better understanding of how the presence of noncondensables affects the flow stability, we performed linear stability calculations similar to those by Priede and Gerbeth[29] and Mercier and Normand,[38] using $Bo_D = 0.72$, $Pr = 9.2$ and the expression for a wavenumber-dependent Biot number derived by Chauvet *et al.*[39] The dependence of Bi on the composition of the gas phase can be obtained in explicit form using Clausius-Clapeyron equation

$$Bi = q\bar{h}\left[\frac{C_a k_a + (1 - C_a)k_v}{k_l} + \frac{1 - C_a}{C_a}\left(\frac{L}{R_v T_0}\right)^2 \frac{D_0 p_0}{k_l T_0}\right], \tag{5}$$

where k is the thermal conductivity, D the binary diffusion coefficient, R the specific gas constant, p the total pressure, and L the latent heat of vaporization, while the subscripts indicate air (a), liquid (l), vapor (v), and reference, i.e., ambient, conditions (0). The analysis is based on solving a boundary-value problem involving two coupled partial differential equations for perturbations, relative to the base solution (4), of the temperature $\theta(x,z,t) = \Theta(z)\exp\{\alpha t - iqx\}$ and stream function $\psi(x,z,t) = \Psi(z)\exp\{\alpha t - iqx\}$ in the liquid layer. The boundary-value problem defines both the vertical profiles $\Theta(z)$ and $\Psi(z)$ of the perturbations and the growth rate $\alpha = \beta + i\omega$ as a function of the (complex) wavenumber $q = \kappa + is$ and all of the nondimensional parameters. The asymptotic amplitude of the perturbations is determined by the strength of convection cell A that exists for all ΔT near the hot wall and the value of s defines the spatial attenuation of the perturbation (or the number of convection cells). The threshold values of Ma_i and the wavenumber $\kappa = 2\pi/\lambda_x$ are found by requiring the perturbation to be critical (i.e., $\beta = 0$) and stationary (i.e., $\omega = 0$). The solutions of the boundary value problem were found using Matlab 2013a (specifically, the function bvp5c) and validated by reproducing the data of Priede and Gerbeth[29] for the $Pr = 13.9$ silicone oil (with $Bi = 0$ and $s = 0$).

As Fig. 20 illustrates, linear stability gives reasonable predictions for the critical Ma_i for transitions from SUF to PMC (which corresponds to $s = (\bar{h})^{-1}$) and from PMC to SMC (which corresponds to $s = (\Gamma_x \bar{h})^{-1}$) in the entire range of C_a considered here. It should be noted, however, that the analysis of Chauvet *et al.*[39] on which the expression (5) is based accounts for the diffusion

of heat and vapor in the gas phase, but ignores advection, so perfect agreement is not expected. For instance, at atmospheric conditions, the critical wavenumber $\lambda_x/\bar{h} = 1.86$ predicted by linear stability analysis for the threshold of SMC is lower, while the critical $Ma_i = 481$ is higher than the values found experimentally (respectively, 2.2 and 430).

Our linear stability calculations show that the critical Ma_i is very weakly dependent on Bo_D over the limited range of (estimated) values studied here ($0.56 \leq Bo_D \leq 0.82$). Indeed, at $Bo_D = O(1)$ and C_a exceeding ~4%, thermocapillary stresses are significantly stronger than buoyancy.[27] Furthermore, buoyancy should play a stabilizing role (the temperature at the top of the liquid layer is higher than at the bottom) and so cannot be responsible for the transitions. Hence, thermocapillary stresses are expected to determine both the structure of the base flow and its stability. Thermocapillary stresses depend on the interfacial temperature profile, which is a function of the composition of the gas phase. Hence, noncondensables should play an important role in the transition between different flow regimes. Since the average temperature gradient τ_i is only weakly dependent on C_a, the effect of noncondensables on the flow stability is described mainly by the variation of the Biot number. The first term in (5) describes the change in the thermal conductivity of the gas phase with C_a. This term, however, is only significant when the gas phase is dominated by noncondensables. At lower C_a, the second term in (5), which describes the effect of latent heat released or absorbed at the interface due to phase change, is dominant. Hence, the increase in Ma_i at lower concentrations of noncondensables is due primarily to the enhancement of phase change and a resulting decrease in the variation in the interfacial temperature gradients about average.

V. CONCLUSIONS

Buoyancy-thermocapillary convection in a layer of a volatile silicone oil subjected to a horizontal temperature gradient was investigated experimentally under a vapor space containing 14%–96% air at pressures ranging from 4.8 kPa to 101 kPa, respectively. The spatially averaged velocity data were curve-fit to an analytical solution for steady uniform flow to estimate the average layer depth and interfacial temperature gradient. Based on these estimates, the interfacial Marangoni number was determined for a range of flow regimes. The results for ambient conditions (i.e., 96% air) are in qualitative agreement with other experimental and numerical studies. An analysis of the velocity field of the oscillatory state suggests that its time scales are consistent with a convective instability of the thermal boundary layer which forms at the free surface next to the heated end of the test cell.

The average concentration C_a of noncondensables appears to have little effect on the base flow, at least over the range of C_a considered here. The average concentration does, however, have a major effect on flow stability, and the critical Marangoni numbers for transition between the various flow states (SUF, PMC, SMC, and OMC) increase as C_a decreases, in surprisingly good agreement with the predictions of linear stability analysis. For example, unsteady flow is only observed in convection under ambient conditions, and the steady multicellular state is only observed for convection at the two higher air concentrations.

Related numerical and analytical studies show that description of the flow in the liquid layer and its stability at reduced concentrations of air requires detailed description of bulk mass transport in the vapor (space), which is a *binary* mixture (i.e., air and vapor), and cannot be understood by simply using the momentum, heat, and mass balance at the liquid-vapor interface. This is especially true in situations where air has been almost completely evacuated (as is the case in many evaporative cooling applications). Linear stability analysis shows that both the latent heat associated with phase change and the heat transfer in the vapor space affect the flow stability. In particular, reducing the concentration of noncondensables enhances phase change, thereby suppressing transitions to more complex convective patterns.

ACKNOWLEDGMENTS

This work was sponsored by the Thermal Management Program of the Office of Naval Research under Award No. N00014-09-1-0298. The authors thank Benjamin M. Chan for his help with the experiments and Tongran Qin for his valuable comments.

[1] R. Mahajan, C.-P. Chiu, and G. Chrysler, "Cooling a microprocessor chip," Proc. IEEE **94**, 1476 (2006).
[2] G. P. Peterson, *An Introduction to Heat Pipes: Modeling, Testing, and Applications* (Wiley, New York, 1994).
[3] C. B. Sobhan, R. L. Rag, and G. P. Peterson, "A review and comparative study of the investigations on micro heat pipes," Int. J. Energy Res. **31**, 664 (2007).
[4] Y. Zhang and A. Faghri, "Advances and unsolved issues in pulsating heat pipes," Heat Transfer Eng. **29**, 20 (2008).
[5] H. B. Ma, B. Borgmeyer, P. Cheng, and Y. Zhang, "Heat transport capability in an oscillating heat pipe," J. Heat Transfer **130**, 081501 (2008).
[6] R. Savino and D. Paterna, "Marangoni effect and heat pipe dry-out," Phys. Fluids **18**, 118103 (2006).
[7] M. F. Schatz and G. P. Neitzel, "Experiments on thermocapillary instabilities," Annu. Rev. Fluid Mech. **33**, 93 (2001).
[8] R. J. Riley and G. P. Neitzel, "Instability of thermocapillary-buoyancy convection in shallow layers. Part 1. Characterization of steady and oscillatory instabilities," J. Fluid Mech. **359**, 143 (1998).
[9] C. De Saedeleer, A. Garcimartin, G. Chavepeyer, J. K. Platten, and G. Lebon, "The instability of a liquid layer heated from the side when the upper surface is open to air," Phys. Fluids **8**, 670 (1996).
[10] J. Burguete, N. Mukolobwiez, F. Daviaud, N. Garnier, and A. Chiffaudel, "Buoyant-thermocapillary convection instabilities in extended liquid layers subject to a horizontal temperature gradient," Phys. Fluids **13**, 2773 (2001).
[11] C. L. Chan and C. F. Chen, "Effect of gravity on the stability of thermocapillary convection in a horizontal fluid layer," J. Fluid Mech. **647**, 91 (2010).
[12] M. K. Smith and S. H. Davis, "Instabilities of dynamic thermocapillary layers. Part 1. Convective instabilities," J. Fluid Mech. **132**, 119 (1983).
[13] M. G. Braunsfurth and G. M. Homsy, "Combined buoyancy-thermocapillary convection in a cavity. Part II. An experimental study," Phys. Fluids **9**, 1277 (1997).
[14] D. Villers and J. K. Platten, "Coupled buoyancy and Marangoni convection in acetone: Experiments and comparison with numerical simulations," J. Fluid Mech. **234**, 487 (1992).
[15] P. Gillon and G. M. Homsy, "Combined buoyancy-thermocapillary convection in a cavity: An experimental study," Phys. Fluids **8**, 2953 (1996).
[16] Z. Q. Zhu and Q.-S. Liu, "Coupling of thermocapillary convection and evaporation effect in a liquid layer when the evaporating interface is open to air," Chin. Sci. Bull. **55**, 233 (2010).
[17] A. Garcimartín, N. Mukolobwiez, and F. Daviaud, "Origin of waves in surface-tension-driven convection," Phys. Rev. E **56**, 1699 (1997).
[18] Y. Ji, Q.-S. Liu, and R. Liu, "Coupling of evaporation and thermocapillary convection in a liquid layer with mass and heat exchanging interface," Chin. Phys. Lett. **25**, 608 (2008).
[19] C. L. Yaws, *Yaws' Handbook of Thermodynamic and Physical Properties of Chemical Compounds: Physical, Thermodynamic and Transport Properties for 5,000 Organic Chemical Compounds* (Knovel, Norwich, NY, 2003).
[20] J. Canny, "A computational approach to edge detection," IEEE Trans. Pattern Anal. Mach. Intell. **8**, 679 (1986).
[21] J. Westerweel and D. Dabiri, "The effect of a discrete window offset on the accuracy of cross-correlation analysis of digital PIV recordings," Exp. Fluids **23**, 20 (1997).
[22] R. D. Keane and R. J. Adrian, "Optimization of particle image velocimeters. Part I: Double pulsed systems," Meas. Sci. Technol. **1**, 1202 (1990).
[23] J. Westerweel and F. Scarano, "Universal outlier detection for PIV data," Exp. Fluids **39**, 1096 (2005).
[24] Y. Li and M. Yoda, "Convection driven by a horizontal temperature gradient in a confined aqueous surfactant solution: The effect of noncondensables," Exp. Fluids **55**(1), 1663 (2014).
[25] R. V. Birikh, "Thermocapillary convection in a horizontal layer of liquid," J. Appl. Mech. Tech. Phys. **7**, 43 (1966).
[26] T. Qin, Z. Tukovic, and R. O. Grigoriev, "Buoyancy-thermocapillary convection of volatile fluids under ambient conditions," Int. J. Heat Mass Transfer **75**, 284 (2014).
[27] T. Qin, Z. Tukovic, and R. O. Grigoriev, "Buoyancy-thermocapillary convection of volatile fluids under their vapors," Int. J. Heat Mass Transfer **80**, 38 (2015).
[28] J.-F. Mercier and C. Normand, "Buoyant-thermocapillary instabilities of differentially heated liquid layers," Phys. Fluids **8**, 1433 (1996).
[29] J. Priede and G. Gerbeth, "Convective, absolute and global instabilities of thermocapillary-buoyancy convection in extended layers," Phys. Rev. E **56**, 4187 (1997).
[30] R. J. Adrian and J. Westerweel, *Particle Image Velocimetry* (Cambridge University Press, New York, 2011).
[31] A. B. Ezersky, A. Garcimartín, J. Burgete, H. L. Mancini, and C. Pérez-García, "Hydrothermal waves in Marangoni convection in a cylindrical container," Phys. Rev. E **47**, 1126 (1993).
[32] V. M. Shevtsova, A. A. Nepomnyashchy, and J. C. Legros, "Thermocapillary-buoyancy convection in a shallow cavity heated from the side," Phys. Rev. E **67**, 066308 (2003).
[33] H. Ben Hadid and B. Roux, "Buoyancy- and thermocapillary-driven flows in differentially heated cavities for low-Prandtl-number fluids," J. Fluid Mech. **235**, 1 (1992).
[34] T. Qin and R. O. Grigoriev, "The effect of noncondensables on thermocapillary-buoyancy convection in volatile fluids," in *Proceedings of the 11th AIAA/ASME Joint Thermophysics and Heat Transfer Conference*, AIAA Paper No. 2014–1898558, 2014.
[35] P. M. Parmentier, V. C. Regnier, and G. Lebon, "Buoyant-thermocapillary instabilities in medium-Prandtl-number fluid layers subject to a horizontal temperature gradient," Int. J. Heat Mass Transfer **36**, 2417 (1993).

[36] T. Qin, M. Yoda, and R. O. Grigoriev, "The effect of noncondensables on buoyancy-thermocapillary convection in confined volatile fluids," in *Proceedings of the ASME 2014 International Mechanical Engineering Congress and Exposition, IMECE2014–40124* (2014).
[37] M. Barthes, C. Reynard, R. Santini, and L. Tadrist, "Non-condensable gas influence on the Marangoni convection during a single vapour bubble growth in a subcooled liquid," Europhys. Lett. **77**, 14001 (2007).
[38] J.-F. Mercier and C. Normand, "Influence of the Prandtl number on the location of recirculation eddies in thermocapillary flows," Int. J. Heat Mass Transfer **45**, 793 (2002).
[39] F. Chauvet, S. Dehaeck, and P. Colinet, "Threshold of Bènard-Marangoni instability in drying liquid films," Europhys. Lett. **99**, 34001 (2012).